

# Target Discrimination and Classification in <sup>1</sup> Through-the-Wall Radar Imaging

Christian Debes<sup>†</sup>, Jürgen Hahn<sup>†</sup>, Abdelhak M. Zoubir<sup>†</sup> and Moeness G. Amin<sup>‡</sup>

<sup>†</sup> Signal Processing Group, Institute of  
Telecommunications  
Technische Universität Darmstadt  
Merckstr. 25  
64283 Darmstadt, Germany  
E-mail: {cdebes, jhahn, zoubir}@spg.tu-darmstadt.de

<sup>‡</sup> Radar Imaging Lab, Center for Advanced  
Communications  
Villanova University  
800 Lancaster Ave.  
Villanova PA 19085, USA  
E-mail: moeness.amin@villanova.edu

## Abstract

In this paper, a scheme for target discrimination and classification is proposed. The proposed scheme is applied to through-the-wall microwave images obtained by using a wideband radar implementing frequency-domain back-projection. We consider stationary targets where Doppler and change-detection based techniques are inapplicable. The proposed scheme applies image segmentation, followed by feature extraction. We map target returns to a feature space, where discrimination among different targets and clutter is performed. To achieve target-clutter discriminations independent of target location in range and cross-range, we use compensation methods to account for varying system resolution within the perimeter of the scene imaged. Real data collected using an indoor radar imaging scanner is used for validation of performance.

**Keywords:** Through-the-wall, radar imaging, segmentation, feature extraction

## I. INTRODUCTION

Through-the-Wall Radar Imaging (TWRI) is an evolving technology[1], [2], [3], [4] allowing to sense through visually opaque building material and man made structures using electromagnetic wave propagation. Having numerous civilian, law enforcement and military applications, TWRI is faced with many challenges, including detection and classification of a large variety of possible indoor targets in presence of multipaths and unwanted wall signal attenuation and dispersive effects [5]. In absence of frequency-domain or time-domain changes associated with target motion, Doppler signatures and change detection techniques applied to non-moving animate and inanimate targets become ineffective to render proper decisions on stationary targets behind walls.

The work by Moeness Amin is supported in part by ONR, Grant no N00014-07-C-0413

The TWRI images of stationary targets are subject to strong artifacts, which could visually<sup>2</sup> appear, in intensity and spatial concentration, as targets. This, in turn, leads to false alarms and misinterpretation of the image. Robust computer-based systematic tests and methods should, therefore, be sought out and applied in lieu of human reading and eye-based inspections.

Much work has been accomplished in modeling and imaging of fixed targets behind walls and inside enclosed structures [6], [7], [8], [9]. Mainly, target detection in through wall imaging has proceeded along two tracks. Data-domain target detection involved waveform design using matched illumination techniques and incorporated partial or full prior knowledge of target RCS over angle and frequency [10]. Matched illumination detection only works well under specific assumptions on targets and propagation environments and becomes less effective with multiple targets and unknown target orientations. Image-domain target detection, on the other hand [11], [12] faces the challenge of operating with limited bandwidth and insufficient physical or synthesized array aperture thus disallowing high resolution based target analyses and classifications. Restrictions on the radar, in terms of size and frequencies, stem from logistics of operation, which includes infeasible long aperture, the need to avoid infringing over wireless services, and responding to wall electrical properties that cause severe attenuation of high frequency signal components. Nevertheless, image-domain detection is considered attractive, as it handles multiple targets and makes no prior assumptions on target RCS.

Detection in the image-domain has been proposed using centralized [13] as well as decentralized [14] frameworks. The common aim within both frameworks is to deduce from a set of  $M$  three-dimensional (3D) TWRI images a single binary 3D reference image indicating the presence or absence of targets.

In this paper, we focus on the problem of target classification. The 3D TWRI image is divided into a finite set of segmented objects which are labelled according to a certain class. This class may depend on target material, shape, etc. This process, referred to as object occupancy map, can then be used to describe the targets present in the scene. A key issue concerning target classification is robustness with respect to target position coordinates and system parameters.

TWRI target images change in pixel intensity and extent when repositioning the target

with respect to the imaging system and/or changing the system parameters, such as band<sup>3</sup>width and aperture. In order to insure that the performance of the detection/classification schemes are robust to system specifications or target positions, the above changes must be properly characterized and taken into consideration. Changes in the TWRI target images can mathematically be expressed by using the concept of the system point spread function (PSF), which is a function of system parameters, such as bandwidth and aperture, as well as the target and standoff distance. The PSF spread determines the dispersion of point targets in the image domain. We propose using the PSF to perform the necessary compensation and to obtain features that are resolution-independent.

Previous work on target classification in TWRI, includes the use of the principal component analysis on B-Scans [15] and superquadric fitting [16] on segmented objects. Both approaches, however, provide features that are not system resolution-independent or target position-invariant. This corresponds to the implicit assumption of imaging in the far field, which is not appropriate for most indoor imaging scenarios. The contribution of this paper is the treatment of a general 3D image domain based target classification scheme for TWRI with resolution-independent features. The proposed classification framework can be of value also for other near-field imaging applications, such as synthetic aperture sonar imaging [17], [18], in which case the target and shadow features depend on the imaging system and scene parameters. It is noted, however, that in this paper the focus is on 3D near-field image classification for indoor radar imaging.

In this paper, we present a classification framework which comprises beamforming, segmentation, feature extraction and finally classification, as shown in Figure 1. In Section II, image formation in radar imaging using wideband sum-and-delay beamforming is summarized. We examine the effect of changes in downrange and crossrange resolution as well as the target-system distance separation on the imaged target pixel intensities and shape. This is fundamental in order to achieve resolution-independent classifications. Section III details different ways of segmenting TWRI images into a finite number of candidate objects. With the objects identified, the next step of feature extraction is described in Section IV. This step maps objects from the image domain to a feature vector which is a parsimonious object description. We consider statistical as well as geometrical feature extractions. A description

of how to perform discrimination between the target of interest and clutter returns is provided<sup>4</sup> in Section V. Finally, the conclusion is given in Section VI. All real data examples, included in this paper are obtained from TWRI measurements collected at the Radar Imaging Lab at Villanova University, Villanova, PA, USA.

## II. IMAGE FORMATION

In this section, the wideband sum-and-delay beamformer [9], [7] for high resolution radar imaging is described. We hereby follow the same scheme as in [9], which has a strong link to high resolution image reconstruction in inverse synthetic aperture radar (ISAR) [19], [20]. In order to achieve position- and resolution-independent features of objects, i.e., insensitivity to changes in object position and system resolution, it is important to examine the effects of the system resolution on the radar image, when using wideband sum-and-delay beamforming. These effects impact pixel intensity values and the appearance of the imaged object. Further, we describe the change of the beamformer when a wall, with known thickness and dielectric constant, is present between the imaging system and the scene of interest. We introduce the experimental setup and demonstrate practical examples of the change of target pixel intensity and object shape, derived theoretically in the first part of this section.

We note that, for through wall radar applications and examples furnished in this paper, we assume perfect knowledge or correct estimated values of the wall parameters. Estimation techniques of the wall thickness and dielectric constant can be found in [2], [3] and references therein.

### A. High resolution radar imaging

In the following, we consider a uniform 1D monostatic array of  $K$  transceivers, placed at  $v_k$ ,  $k = 0, \dots, K - 1$ . The scene is described by a local coordinate system  $(u', v')$ , as shown in Figure 2. The distance from the  $k$ -th transceiver can be approximated by

$$R_k(u', v') \approx R_k(0, 0) + u' \cos \varphi_k - v' \sin \varphi_k \quad (1)$$

where  $R_k(0, 0)$  denotes the distance from the  $k$ -th transceiver to the center of the scene, and  $\varphi_k$  is the respective angle. Accordingly,

$$\varphi_k = \sin^{-1} \left( \frac{v_k}{R_k(0, 0)} \right) \quad (2)$$

where  $v_k$  is the position of the  $k$ -th transceiver with respect to the array center. As such, the two-way propagation delay is given by,

$$\tau_k(u', v') \approx \frac{2}{c} (R_k(0, 0) + u' \cos \varphi_k - v' \sin \varphi_k) \quad (3)$$

with  $c$  denoting the propagation speed. Consider a single point target present at  $(u'_p, v'_p)$ . Similar to Equation (3), the distance from the target to the  $k$ -th transceiver and the corresponding two-way propagation delay are, respectively, given by,

$$R_k(u'_p, v'_p) \approx R_k(0, 0) + u'_p \cos \varphi_k - v'_p \sin \varphi_k \quad (4)$$

$$\tau_k(u'_p, v'_p) \approx \frac{2}{c} (R_k(0, 0) + u'_p \cos \varphi_k - v'_p \sin \varphi_k) \quad (5)$$

Image formation can be performed using time-domain or frequency-domain backprojections, depending on the transmitted signal form. When using the stepped-frequency (SF) approach, a wideband pulse is approximated by a finite number of narrowband pulses. Advantages of the step-frequency based imaging are multifold, as discussed in [7]. In the following, we adopt the SF approach. The experimental data used in our examples were generated by a SF 2D scanner. It is noted, however, that the performance of the proposed segmentation and feature extraction techniques is independent of whether time-domain pulsing or step-frequency transmission is employed. The image formation using a sum-and-delay beamformer is,

$$I(u', v') = \sum_{p=0}^{P-1} \sum_{l=0}^{L-1} \sum_{k=0}^{K-1} \Gamma(u'_p, v'_p) e^{-j\omega_l(\tau_k(u', v') - \tau_k(u'_p, v'_p))} \quad (6)$$

where  $\omega_l$  is the  $l$ -th frequency bin and  $P$ ,  $L$  and  $K$  denote the number of targets, frequency bins, and array elements, respectively. Further,  $\Gamma(u'_p, v'_p)$  is the complex reflectivity of the  $p$ -th target. The invariance of  $\Gamma$  with frequency and antenna elements is the characteristics of

point targets. Reducing the problem to the case of a single target at  $(u'_0, v'_0)$  yields,

$$I(u', v') = \Gamma(u'_0, v'_0) \sum_{l=0}^{L-1} \sum_{k=0}^{K-1} e^{-j\omega_l(\tau_k(u', v') - \tau_k(u'_0, v'_0))} \quad (7)$$

$$= \Gamma(u'_0, v'_0) \sum_{l=0}^{L-1} \sum_{k=0}^{K-1} e^{-j\frac{2\omega_l}{c}((u' - u'_0) \cos \varphi_k - (v' - v'_0) \sin \varphi_k)} \quad (8)$$

Using the notation  $\omega_l = \omega_0 + l\Delta\omega$ , where  $\omega_0$  is the lowest frequency employed, the acquired complex image can be written as

$$\begin{aligned} I(u', v') &= \Gamma(u'_0, v'_0) \sum_{l=0}^{L-1} \sum_{k=0}^{K-1} e^{-j\frac{2(\omega_0 + l\Delta\omega)}{c}((u' - u'_0) \cos \varphi_k - (v' - v'_0) \sin \varphi_k)} \\ &= \Gamma(u'_0, v'_0) \sum_{l=0}^{L-1} \sum_{k=0}^{K-1} e^{-j\frac{2\omega_0}{c}((u' - u'_0) \cos \varphi_k - (v' - v'_0) \sin \varphi_k)} e^{-j\frac{2l\Delta\omega}{c}((u' - u'_0) \cos \varphi_k - (v' - v'_0) \sin \varphi_k)} \\ &= \Gamma(u'_0, v'_0) \sum_{k=0}^{K-1} e^{-j\frac{2\omega_0}{c}((u' - u'_0) \cos \varphi_k - (v' - v'_0) \sin \varphi_k)} \sum_{l=0}^{L-1} e^{-j\frac{2l\Delta\omega}{c}((u' - u'_0) \cos \varphi_k - (v' - v'_0) \sin \varphi_k)} \\ &= \Gamma(u'_0, v'_0) \sum_{k=0}^{K-1} e^{-j\frac{2\omega_0}{c}((u' - u'_0) \cos \varphi_k - (v' - v'_0) \sin \varphi_k)} e^{-j\frac{(L-1)\Delta\omega}{c}((u' - u'_0) \cos \varphi_k - (v' - v'_0) \sin \varphi_k)} \times \\ &\quad \frac{\sin\left(\frac{L\Delta\omega}{c}((u' - u'_0) \cos \varphi_k - (v' - v'_0) \sin \varphi_k)\right)}{\sin\left(\frac{\Delta\omega}{c}((u' - u'_0) \cos \varphi_k - (v' - v'_0) \sin \varphi_k)\right)} \end{aligned} \quad (9)$$

Let  $P(u', v')$  denote the system point spread function (PSF), given by

$$P(u', v') = \sum_{k=0}^{K-1} \frac{\sin\left(\frac{L\Delta\omega}{c}\xi_k(u', v')\right)}{\sin\left(\frac{\Delta\omega}{c}\xi_k(u', v')\right)} \exp\left(-j\left(\frac{2\omega_0}{c} + \frac{(L+1)\Delta\omega}{c}\right)\xi_k(u', v')\right) \quad (10)$$

where  $\xi_k(u', v') = u' \cos \phi_k - v' \sin \phi_k$ . Using this notation, the acquired radar image can be written as a convolution of the target reflectivity with the system point spread function as,

$$I(u', v') = \Gamma(u', v') \star \star P(u', v') \quad (11)$$

where  $\star\star$  denotes the two-dimensional convolution. The PSF is of fundamental importance in examining the effect of resolution on the resulting target images. Considering Equation (10), the PSF is a function of the signal bandwidth and the number of array elements, thus affecting resolution in downrange and crossrange. For a derivation of the PSF for TWRI in far-field scenarios using ultrawideband signals we refer to [21].

Examples of a PSF are shown in Figure 3. Here, we considered imaging a  $30 \times 30$  feet

region with its center being at 100 feet away from the imaging system. The antenna elements are centered around  $v = 0$ ft with an interelement spacing of 4in. A step-frequency approach, as described above, is considered with a starting frequency  $\omega_0 = 0.8$ GHz and a frequency spacing of  $\Delta\omega = 5$ MHz. Figure 3 illustrates the PSF for 51, 101 and 401 antenna elements as well as 201, 401 and 801 frequency steps. As can be clearly observed, the extent of the PSF in range is determined by the bandwidth, whereas its extent in crossrange is guided by the number of array elements.

### B. Effect of the change of resolution

We consider the image at the target position which according to Equation (6) i

$$I(u'_0, v'_0) = \lim_{\substack{u' \rightarrow u'_0 \\ v' \rightarrow v'_0}} I(u', v') = K \cdot L \cdot \Gamma(u'_0, v'_0) \quad (12)$$

Accordingly, the magnitude image at the target position, which will be used in subsequent sections, is then

$$|I(u'_0, v'_0)| = KL \cdot |\Gamma(u'_0, v'_0)| \quad (13)$$

The above equation simply states that, for the simple scenario of a point target, an increase in the number of array antennas and/or the number of step frequencies results in a linear scaling of the pixel intensity. If the interelement spacing and frequency spacing remain constant, then the above increase in antennas or frequencies, respectively, amounts to increasing the array aperture and bandwidth, and as such, represents an imaging system with enhanced crossrange and range resolution capabilities.

The pixel intensity at target positions is not only dependent on  $L$  and  $K$ , but also on the scene center distance  $R_k(0, 0)$ . From basic radar principles [22] it is known that the amplitude of target reflections is inverse proportionally to the range square.

Table I summarizes the three system and scene parameters treated in this Section, i.e., bandwidth, array elements, and target distance and lists the effect on the image in terms of pixel intensity and target image extent. It is noted that an exact closed form expression of the summation (10) as a function of the system parameters and target position is very difficult to obtain. In the following, we examine the properties of the PSF through numerical evaluation of Equation (10).

Figure 4(a) and (b) shows slices through the 2D PSF at zero range and crossrange, respectively. The same setup as described previously was considered. As can be seen, an increase in bandwidth or number of array elements yields an increase in the maximum PSF value as well as a narrower mainlobe. Figures 5(a) and (b) plot the maximum PSF value as a function of the number of array elements and bandwidth and demonstrates the linear relationship as dictated by Equation (13).

Consider the 3dB width of the PSF mainlobe. This is used as a resolution measure and indicates the dispersion of a point target in the image as well as the degree of smoothness of a spatially-extended target in the image domain. Figures 6(a), (b) and (c) plot the PSF spread in range and crossrange for different number of array elements, bandwidths and scene center distance, respectively. It is evident that the 3dB bandwidth of the PSF decreases with increased array aperture and signal bandwidth. It is, however, proportional to the target range.

Changing parameter	Yields
Increased Bandwidth	Increased Pixel intensity
	Decreased target image extent in range
Increased number of array elements	Increased Pixel intensity
	Decreased target image extent in crossrange
Increased target distance	Decreased pixel intensity
	Increased target image extent in range/crossrange

TABLE I  
EFFECT OF SYSTEM OR SCENE PARAMETERS ON THE RADAR IMAGE

### C. Through-the-Wall Radar Imaging

In wideband sum-and-delay beamforming for TWRI [7], the summation over all frequencies and array elements still holds as per Equation (6), but the delay from the  $k$ -th array element to a point  $(u', v')$  in the local scene coordinate system now has to incorporate the propagation through the wall as [7]

$$\tau_{k,\text{wall}}(u', v') = (R_{\text{air},1} + \sqrt{\epsilon}R_{\text{wall}} + R_{\text{air},2})/c \quad (14)$$

where  $\epsilon$  denotes the dielectric constant of the wall and  $R_{\text{air},1}$ ,  $R_{\text{wall}}$  and  $R_{\text{air},2}$  represent respectively the traveling distances of the electromagnetic wave before, through, and behind the wall.



We note that for known wall parameters, the use of Equation (14) instead of the free-space equivalent in Equation (3) has no effect on the conclusions drawn above regarding the change of the target images. It is noted that for more complicated wall structures and frequency-dependent wall parameters, the PSF becomes more involved and cannot straightforwardly be obtained by replacing the focusing delay in Equation (6).

The imaging system used throughout this paper is a synthetic aperture radar system [23], where a single horn antenna, in motion, synthesizes a  $57 \times 57$  element planar array. The interelement spacing is  $0.875in$ . As described above, a continuous-wave stepped-frequency signal is used to approximate a wideband pulse. The experimental setup is depicted in Figure 7, where a metal dihedral is placed on a high foam column behind a wooden wall of thickness  $2in$ . To examine the effect of target image change with increasing range, the dihedral is placed at three different positions. These are 4, 7 and 11 feet away from the array center. Further, four different bandwidths, namely 0.3, 0.5, 0.7 and 1.0 GHz are used with a center frequency of 1.5 GHz to illuminate the scene. Choosing a step size of 5 MHz yields 61, 101, 141 and 201 frequency steps, respectively.

The resulting B-Scan images (two-dimensional cuts through the 3D volume) at the height of the target center are shown in Figure 8. For imaging, we used background subtraction [7], [11] and known wall parameters. The effect of changing the resolution via bandwidth or target distance can be observed as explained in the first part of this Section. Increasing the target distance yields blurring in range, whereas increasing the bandwidth yields focussing in range.

### III. RADAR IMAGE SEGMENTATION

For a two-dimensional array, the output of TWRI, as considered in Section II, is a complex 3D image, representing the target reflectivity in the scene of interest. In the following, we provide algorithms for image segmentation and feature extraction, and perform discrimination in the image domain. Let  $Y(i, j, h)$  with  $0 \leq i < N_i$ ,  $0 \leq j < N_j$  and  $0 \leq h < N_h$  denote the absolute value of the 3D image with  $Y(i, j, h) \geq 0$ , whereby  $N_i$ ,  $N_j$  and  $N_h$  are the number of voxels in range, crossrange (azimuth) and height (elevation), respectively.

Segmentation is the first step of the classification chain introduced in Figure 1. Given a set of labels  $\mathcal{G}$ , the aim is to assign a label  $x \in \mathcal{G}$  to each voxel  $Y(i, j, h)$ ,  $0 \leq i < N_i$ ,

$0 \leq j < N_j$ ,  $0 \leq h < N_h$ . For TWRI applications, we consider  $\mathcal{G} = \{0; 1\}$ , i.e., each voxel<sup>10</sup> is assigned to belong to either background ( $x = 0$ ) or target ( $x = 1$ ).

We consider two common and widely used segmentation algorithms, the Iterated Conditional Modes (ICM) [24] and the Levelset Method (LSM) [25]. We form vectorized through wall radar images, where the elements are in lexicographic notation. A 3D image is thus represented as a vector  $\mathbf{y}$ , where  $y_n$  denotes its  $n$ -th element,  $n = 0, \dots, N-1$ , with  $N = N_i \cdot N_j \cdot N_h$ .

#### A. Segmentation using ICM

The ICM algorithm was initially proposed by Besag in 1986 [24] as a method to clean images. Over the past several years, it has extensively been used as a segmentation tool. In cases where the pdf classes for the different segments are known [26], [27], [28], [29], [30], ICM proves to be an effective and computationally attractive method. Let  $\mathbf{x}$  denote the true underlying label field with  $x_n$  denoting its  $n$ -th element,  $n = 0, \dots, N-1$  and  $x_n \in [0; 1]$ . Using a maximum *a posteriori* (MAP) approach,  $\mathbf{x}$  can be estimated as

$$\hat{\mathbf{x}} = \arg \max_{\mathbf{x}} \{p(\mathbf{x} | \mathbf{y})\} \quad (15)$$

which, using Bayes' theorem and assuming conditional independence, can be written as

$$\hat{\mathbf{x}} = \arg \max_{\mathbf{x}} \{p(\mathbf{x})p(\mathbf{y} | \mathbf{x})\} = \arg \max_{\mathbf{x}} \left\{ \prod_{n=0}^{N-1} p(x_n)p(y_n|x_n) \right\} \quad (16)$$

Here,  $p(\mathbf{y} | \mathbf{x})$  is a conditional distribution which can be chosen according to the pdf class of the different segments, and  $p(\mathbf{x})$  denotes the prior. Using the Markovian property [31],  $p(x_n)$  can be simplified by assuming that the prior probability of a voxel  $x_n$  only depends on its neighborhood rather than the whole image, e.g.,

$$p(x_n) = \exp(\varrho \# \{x_t \in \mathcal{N}_{x_n} | x_t = x_n\}) \quad (17)$$

where  $\varrho > 0$  is the so called attraction parameter,  $\#\{\cdot\}$  denotes the cardinal number of the set and  $\mathcal{N}_{x_n}$  is the neighborhood of element  $x_n$ . It is noted, that the assumption of independence in Equation (16) is only an approximation as the width of the point spread function yields correlation in the measurement of neighboring samples.

The estimate in Equation (16) is calculated iteratively to approximate the MAP estimate.

ICM starts with an initial estimate of the label field  $\mathbf{x}$ , which can, e.g., be obtained via<sup>11</sup> simple thresholding or more advanced methods such as the minimum cross-entropy thresholding technique [32]. A new label field is then obtained by iteratively maximizing the posterior distribution for every voxel, i.e., deciding for the new label  $\hat{x}_n$  which maximizes  $\exp(\varrho \#\{x_t \in \mathcal{N}_{x_n} | x_t = x_n\}) p(y_n | x_n, g_n)$ . The procedure is continued until convergence is achieved.

The question arises is how to choose  $p(y_n | x_n)$  and the neighborhood  $\mathcal{N}_{x_n}$  for the a priori distribution. Considering the 3D neighborhood, different possibilities exist [33], depending on the desired degree of smoothness in the segmented image. In the following, we restrict ourselves to a 26-neighborhood for simplicity, meaning that a voxel depends only on such number of its direct neighbors. Considering the conditional distribution  $p(y_n | x_n)$ , the image formation for TWRI has to be recalled, as per Equation (6). When the scene contains point targets, the image reflectivity at a particular point in space can be modelled as a zero-mean complex random variable where the real and imaginary parts are independently Gaussian distributed with a common variance [34]. The absolute value of the image considered in this and subsequent sections thus follows a Rayleigh distribution. However, it shall be noted that the central limit theorem may not be applicable as the number of array elements and/or frequencies used is too small in practice to permit the Gaussian assumption. Also, Gaussianity may be invalid in imaging scenarios which deviate from the simple scenario treated in Section II, e.g., when considering more complex wall effects, violation of the far-field assumption and/or dealing with extended targets. In the sequel, we therefore consider the Weibull distribution [12], [35] as a generalization of the Rayleigh distribution, allowing more flexibility for data modelling. Thus, the pdf of  $y_n$  is given by

$$p(y_n | x_n) = \frac{\kappa_{x_n}}{\lambda_{x_n}} \left( \frac{y_n}{\lambda_{x_n}} \right)^{\kappa_{x_n}-1} \exp \left\{ - \left( \frac{y_n}{\lambda_{x_n}} \right)^{\kappa_{x_n}} \right\}; \quad y_n \geq 0 \quad (18)$$

where  $\kappa_{x_n}$  and  $\lambda_{x_n}$  are the shape and scale parameters of the Weibull distribution given label  $x_n$ , respectively. In each iteration, these parameters can be estimated for every segment via the maximum likelihood principle as

$$(\kappa_0, \lambda_0) = \arg \max_{(\kappa, \lambda)} \prod_{\{y_n | x_n=0\}} \frac{\kappa}{\lambda} \left( \frac{y_n}{\lambda} \right)^{\kappa-1} \exp \left\{ - \left( \frac{y_n}{\lambda} \right)^{\kappa} \right\} \quad (19)$$

$$(\kappa_1, \lambda_1) = \arg \max_{(\kappa, \lambda)} \prod_{\{y_n | x_n=1\}} \frac{\kappa}{\lambda} \left( \frac{y_n}{\lambda} \right)^{\kappa-1} \exp \left\{ - \left( \frac{y_n}{\lambda} \right)^{\kappa} \right\} \quad (20)^{12}$$

A typical segmentation result of a metal dihedral using the experimental data from Section II are shown in Figure 9(a)-(c). Here, minimum cross entropy thresholding [32] was applied to initialize the segmentation, and attraction parameters  $\varrho \in \{0.1, 1.5, 50\}$  were used. A too small attraction parameter practically neglects neighboring information/image correlation. This generally yields larger segmented objects and may have unwanted effects such as merging of different objects and noise effects. When choosing a very large attraction parameter (see Fig. 9(c)) a large weight is set on neighboring information/image correlation. This yields to small, concentrated objects around the target pixel intensity maximum. Effects of a very large attraction parameter include unwanted splitting of objects with low pixel intensity correlation. The same conclusions hold when the size of the local voxel neighborhood  $\mathcal{N}_{x_n}$  is changed as dictated by Equation (17). Choosing an attraction parameter of  $\varrho = 1.5$  is a typical value that is also used in other imaging applications [24]. It provides a reasonable tradeoff between noise suppression and target distortion.

### B. Segmentation using the Level Set Method

The ICM may not be suitable in all situations, especially when the pdf classes are unknown. The pdf classes in TWRI depend on the imaging system and a large number of potential targets. We therefore consider an alternative segmentation approach, namely the Level Set Method (LSM), which was developed by Osher and Sethian [25]. Instead of relying on statistical models, the LSM is a topology-based approach which makes it a highly attractive tool in volumetric data reconstruction, e.g., in medical image processing.

In contour-based segmentation algorithms, such as the Active Contour Model [36], the contour around one image segment is adapted to best fit to the corresponding image data at hand. This is often achieved by varying the contour in such a way that a predefined energy function is minimized. The key idea of the LSM is to fit a contour in a higher dimensional space. The image segment is considered as the level set of the image plane and a surface of a higher dimensionality. By moving the higher dimensional shape through the image plane, the LSM adapts the image segment contour [25], [37], see Figure 10. One advantage of this method is the capability to easily merge and split segments. Since the LSM theory holds for

arbitrary dimensions, it can directly be applied to three-dimensional TWRI images.

The LSM relies on energy functions to be minimized in a higher dimensional space. Classical energy functions, such as the geodesic contours [38] are based on image derivatives. Radar images, including TWRI, however, do not typically show clear boundaries between target regions and background. The images are rather smoothed, as the image is the result of a 3D convolution of the target reflectivity and the system point spread function. Instead of relying solely on image derivatives, we consider the energy function developed by Zhang et al. [39], which includes image derivatives as well as a contiguous region term which can cope with smooth target regions.

A typical segmentation result using the same example as above is shown in Figure 9(b). For initialization of the LSM, a threshold on the normalized image of 0.3 was chosen, which gave the best result in all cases. It is evident that both segmentation algorithms perform equally well in this scenario.

#### IV. FEATURE EXTRACTION

The output of segmentation is a set of 3D candidate objects which, in the following, are denoted as  $O_q$ ,  $q = 0, \dots, Q - 1$ , with  $Q$  denoting the total number of objects after segmentation. Feature extraction maps each candidate object onto a feature space with a compact representation, in which the object is described by a preferably small number of parameters. In this section, we present two approaches for feature extraction; one is based on statistical features, whereas the other is based on geometrical features. In both cases, it is demonstrated how to map an object on the respective feature space and how to transform the feature vector such that resolution-independent features can be obtained.

##### A. Statistical Features

As detailed in Section III, the Weibull model provides a good match to imaged target characteristics and offers high flexibility to model target returns in TWRI images. Therefore, it becomes intuitive to use the respective distribution parameters  $(\kappa_q, \lambda_q)$ , representing the  $q$ -th object as object descriptors. The parameters  $(\kappa_q, \lambda_q)$  can be estimated via maximum

likelihood, similarly to Equation (20) as,

$$(\kappa_q, \lambda_q) = \arg \max_{(\kappa, \lambda)} \prod_{y_n \in O_q} \frac{\kappa}{\lambda} \left( \frac{y_n}{\lambda} \right)^{\kappa-1} \exp \left\{ - \left( \frac{y_n}{\lambda} \right)^{\kappa} \right\} \quad (21)$$

Note that Equation (21) is computed at convergence of the ICM. It is further important to note that Equation (21) cannot directly be used for target discrimination, since the obtained features are not resolution-independent. Different objects at different locations imaged by different radar systems may have a similar pdf which renders target discrimination unreliable.

As derived in Section II and summarized in Table I, the image intensity is dependent on the bandwidth, the number of array elements and the target distance. Intensity-independent features are provided by choosing

$$(\kappa_q, \lambda_q) = \arg \max_{(\kappa, \lambda)} \prod_{y_n \in O_q} \frac{\kappa}{\lambda} \left( \frac{\tilde{y}_n}{\lambda} \right)^{\kappa-1} \exp \left\{ - \left( \frac{\tilde{y}_n}{\lambda} \right)^{\kappa} \right\} \quad (22)$$

where

$$\tilde{y}_n = \frac{y_n}{\max_q \{y_n\}} \quad (23)$$

with  $\max_q \{y_n\}$  denoting the maximum voxel value in the  $q$ -th object. Practically, this means that each object is normalized before feature extraction such that scaling factors due to system transmitted power are compensated for.

### B. Geometrical Features

Statistical features, such as the parameters of a Weibull distribution, provide important information about an object under test, however, they ignore object features, such as shape, extent in range, crossrange, and height. Superquadrics [40] present an effective method for the geometrical description of 3D objects by few parameters. Superquadrics are used in the sequel as an alternative, or additive, feature representation to that which is statistically based. For simplicity, we restrict ourselves to superellipsoids where the implicit definition, without considering rotation, is given as [40]:

$$F_{SQ}(i, j, h) = \left( \left( \frac{i}{a_i} \right)^{\frac{2}{\epsilon_1}} + \left( \frac{j}{a_j} \right)^{\frac{2}{\epsilon_1}} \right)^{\frac{\epsilon_1}{\epsilon_2}} + \left( \frac{h}{a_h} \right)^{\frac{2}{\epsilon_2}} \quad (24)$$

where  $\epsilon_1$  and  $\epsilon_2$  which influence the circularity are the squareness parameters in east-west and north-south direction, respectively. Most real objects can be assumed to possess a convex shape which means that  $\epsilon_1, \epsilon_2 \in (0, 1]$ . The parameters  $a_i, a_j$  and  $a_h$  denote the size in range, crossrange, and height, respectively.

Let

$$\underline{\phi}_B = (a_i, a_j, a_h, \epsilon_1, \epsilon_2) \quad (25)$$

denote the basic parameter vector of one superquadric without considering rotation. This parameter can be estimated by non-linear least squares fitting as,

$$\hat{\underline{\phi}}_B = \arg \min_{\underline{\phi}} \sum_{i,j,h \in \text{Shell}} \left( \sqrt{a_i a_j a_h} (F_{SQ}(i, j, h; \underline{\phi})^{\epsilon_2} - 1) \right)^2 \quad (26)$$

where the superquadric representation, given a parameter vector  $\underline{\phi}$ , is denoted as  $F_{SQ}(i, j, h; \underline{\phi})$ . The sum is evaluated for all voxels on the object shell, further, scaling by  $\sqrt{a_i a_j a_h}$  and exponentiation by  $\epsilon_2$  is typically applied [41] to avoid local minima. Note that  $F_{SQ}(i, j, h) = 1$  for all voxels on the superquadric shell. Thus, Equation (26) is minimizing the mean square error between the object and the fitted superquadric shell. The optimization problem in Equation (26) can be solved by, e.g., the Levenberg-Marquardt method [42], [43]. Due to the non-linear optimization, the end result of superquadric fitting may strongly depend on the initialization. Proper initialization of the size parameters  $a_i, a_j$  and  $a_h$  is rather a simple task, since the nominal size of the segment in range, crossrange and height can be discerned from the image and used for this purpose. Further, Solina [41] explains that the initial value of the shape parameters  $\epsilon_1, \epsilon_2$  is not critical and suggests the unit value, which would consider an ellipsoid shape for initialization.

*1) Rotation and global deformations:* Equation (24) denotes a simplified superquadric, which may not be suitable to represent the diversity of possible target objects arising in TWRI applications. We extend the above model by considering rotation as well as global deformations to allow a more flexible superquadric fitting.

The rotation is performed by means of the tensor product, represented by a  $3 \times 3$  matrix

$\mathbf{I}_T$  [41] as,

$$\mathbf{I}_T = \frac{1}{N_q} \sum_{(i,j,h) \in O_q} \begin{bmatrix} (j - \bar{j}_q)^2 + (h - \bar{h}_q)^2 & -(j - \bar{j}_q)(i - \bar{i}_q) & -(h - \bar{h}_q)(i - \bar{i}_q) \\ -(i - \bar{i}_q)(j - \bar{j}_q) & (i - \bar{i}_q)^2 + (h - \bar{h}_q)^2 & -(h - \bar{h}_q)(j - \bar{j}_q) \\ -(i - \bar{i}_q)(h - \bar{h}_q) & -(j - \bar{j}_q)(h - \bar{h}_q) & (i - \bar{i}_q)^2 + (j - \bar{j}_q)^2 \end{bmatrix} \quad (27)$$

where  $N_q$  is the number of voxels in the  $q$ -th object and  $(\bar{i}_q, \bar{j}_q, \bar{h}_q)$  is the corresponding center of gravity. The orthogonal rotation matrix  $\mathbf{R}$  is then the matrix that diagonalizes  $\mathbf{I}_T$  as

$$\mathbf{D} = \mathbf{R}^{-1} \mathbf{I}_T \mathbf{R} \quad (28)$$

where  $\mathbf{D}$  is a diagonal matrix. A multiplication by  $\mathbf{R}$  and  $\mathbf{R}^{-1}$  leads to

$$\mathbf{R} \mathbf{D} \mathbf{R}^{-1} = \mathbf{I}_T. \quad (29)$$

Hence,  $\mathbf{R}$  can be computed by eigenvalue decomposition.

The *roll-pitch-yaw* angles, also referred to as *XYZ* angles, are used to represent the rotation of a superquadric. They are denoted as  $\alpha_i, \alpha_j$  and  $\alpha_h$ , representing rotation around the  $i, j$  and  $h$ -axis, respectively. First,  $\alpha_j$  is determined by

$$\alpha_j = \arctan(-\mathbf{R}_{31}, \sqrt{\mathbf{R}_{11}^2 + \mathbf{R}_{21}^2}). \quad (30)$$

where  $\mathbf{R}_{r_1, r_2}$  is the  $(r_1, r_2)$ -th entry in the  $3 \times 3$  rotation matrix and  $\arctan(\cdot, \cdot)$  denotes the two-argument arctangent [44]. The remaining angles are then given as,

$$\alpha_h = \begin{cases} 0, & \alpha_j = \pm\pi/2 \\ \arctan\left(\frac{\mathbf{R}_{21}}{\cos(\alpha_j)}, \frac{\mathbf{R}_{11}}{\cos(\alpha_j)}\right), & \text{otherwise} \end{cases} \quad (31)$$

$$\alpha_i = \begin{cases} \arctan(\mathbf{R}_{12}, \mathbf{R}_{22}), & \alpha_j = \pi/2 \\ -\arctan(\mathbf{R}_{12}, \mathbf{R}_{22}), & \alpha_j = -\pi/2 \\ \arctan\left(\frac{\mathbf{R}_{32}}{\cos(\alpha_j)}, \frac{\mathbf{R}_{33}}{\cos(\alpha_j)}\right), & \text{otherwise} \end{cases} \quad (32)$$

Note that by convention of the *roll-pitch-yaw* angles, an object is first rotated around the  $i$ -axis, then  $j$ -axis and finally  $h$ -axis. The case differentiation is required to avoid singularities.

Though superquadrics can model a large variety of objects, there are shapes that cannot be



fitted, such as cones. In this case, the global deformations tapering and bending can be used,<sup>17</sup> as proposed in [41]. Due to computational complexity, only tapering is considered herein. For tapering along the  $h$ -axis, two new parameters,  $T_i$  and  $T_j$ , are introduced. The coordinates  $(i, j, h)$  have to be transformed as:

$$\begin{aligned} i_{\text{taper}} &= \frac{i}{\frac{T_i}{a_h}h + 1} \\ j_{\text{taper}} &= \frac{j}{\frac{T_j}{a_h}h + 1} \\ h_{\text{taper}} &= h \end{aligned}$$

The order of performing the superquadric fitting steps, translation, rotation, deformation is critical. In general, global deformations should be always performed before translation and rotation [41].

We consider the following extended parameter vector

$$\underline{\phi}_{SQ,R} = (a_i, a_j, a_k, \epsilon_1, \epsilon_2, \alpha_i, \alpha_j, \alpha_h, T_i, T_j) \quad (33)$$

representing all size, shape, rotation and deformation parameters. The parameter vector  $\underline{\phi}_{SQ,R}$  can be estimated via nonlinear Least-Squares Optimization, as in Equation (26).

Again,  $\hat{\underline{\phi}}_{SQ,R}$  cannot directly be used for target discrimination, as the object shape is position- and resolution-dependent. As shown in Section II and summarized in Table I, the target image extent is dependent on the system PSF extent. We thus can obtain resolution-independent features by normalizing the superquadric size parameters as

$$\tilde{a}_i = \frac{a_i}{P_{\text{Crossrange},3dB}} \quad (34)$$

$$\tilde{a}_j = \frac{a_j}{P_{\text{Range},3dB}} \quad (35)$$

$$\tilde{a}_h = \frac{a_h}{P_{\text{Height},3dB}} \quad (36)$$

where  $P_{\text{Crossrange},3dB}$ ,  $P_{\text{Range},3dB}$  and  $P_{\text{Height},3dB}$  denote the (dimensionless) 3dB mainlobe width of the system PSF in crossrange, range and height, respectively. Note that the other parameters, such as rotation, global deformation, and squareness are *per se* resolution-independent and do not need to be compensated for. The final single superquadric parameter vector is thus

denoted as

$$\phi_{SQ} = (\tilde{a}_i, \tilde{a}_j, \tilde{a}_k, \epsilon_1, \epsilon_2, \alpha_i, \alpha_j, \alpha_h, T_i, T_j) \quad (37)$$

It is noted that fitting a single superellipsoid is reasonable given the resolution at hand. For high-resolution radar images, more complicated target models such as free-form deformations [45] or concatenated superquadrics [46] would have to be considered.

## V. TARGET DISCRIMINATION - EXPERIMENTAL RESULTS

We consider the scenario presented in Section II for evaluation of the proposed techniques. It includes a metal dihedral imaged through a wooden wall. Using three different target distance (4, 7 and 11 ft) and four different bandwidths (0.3, 0.5, 0.7 and 1.0 GHz), a total of 12 3D TWRI images are obtained. The same array aperture is used. In what follows, these images are segmented using the Levelset method, although it should be noted that similar results are obtained using the ICM.

Figure 11(a) plots the histograms of the 12 segments, imaged under different resolutions, obtained using kernel density estimation [47]. The histograms differ in scale, as derived earlier in Equation (13). Performing compensation, i.e., normalizing the image data between 0 and 1, yields the histograms in Figure 11(b), which now align and can be used for resolution-independent target discrimination.

As proposed in Section IV, we consider the scale and shape parameters of the Weibull distribution as features to represent an object under test. The results are depicted in Figure 11(c) (uncompensated) and (d) (compensated). Again, it can be observed that the parameter estimates move closer together when using compensation which improves target discrimination.

As an alternative to the statistical feature extraction, we have proposed in Section IV geometrical feature extraction using superquadrics. Two superquadric features, namely the volume and the tapering parameter  $T_i$  are depicted in Figure 12(a). Here, the target volume significantly changes with bandwidth. A small target volume size around 500 voxels is obtained when using 1.0 GHz bandwidth (depicted as green crosses). When reducing the bandwidth to, e.g., 0.3 GHz, the volume increases to approx. 1300 (red crosses). Performing compensation as per Equation (36), we obtain the scatterplot as in Figure 12(b) where the

estimated target volume is concentrated in a small area.

Finally, we consider the problem of discriminating the dihedral object from others, which may be considered as In Figure 13(a), the Weibull parameter estimates are plotted for clutter objects (black crosses) and the dihedrals (blue triangles). Clutter objects stem from various TWRI experiments and include non-dihedral objects such as tables, chairs and other calibration objects. It can be seen that target discrimination is difficult as both classes are spread in the same range. The same holds when considering the superquadric parameters as shown in Figure 13(c). Performing the proposed compensation, we obtain scatterplots as in 13(b) and 13(d), where the dihedral features are now strongly concentrated and discriminable from the clutter returns.

For the task of automatic target classification we consider the resolution-dependent (RD) and resolution-independent (RI) feature vectors

$$\underline{\psi}_{RD} = (\kappa_q, \lambda_q, a_i, a_j, a_k, \epsilon_1, \epsilon_2, \alpha_i, \alpha_j, \alpha_h, T_i, T_j) \quad (38)$$

$$\underline{\psi}_{RI} = (\tilde{\kappa}_q, \tilde{\lambda}_q, \tilde{a}_i, \tilde{a}_j, \tilde{a}_k, \epsilon_1, \epsilon_2, \alpha_i, \alpha_j, \alpha_h, T_i, T_j) \quad (39)$$

which consist of statistical as well as geometrical features. Classification is performed using the Mahalanobis distance [48], assuming the feature vectors  $\underline{\psi}_{RD}$  and  $\underline{\psi}_{RI}$  to follow a multivariate Gaussian distribution, respectively. The setup consists of 1 dihedral, imaged at 12 different system resolutions and 40 clutter objects. The clutter objects are chosen from various 3D TWRI images which do not include dihedrals. A Leave-One-Out approach is considered in which successively one of the 52 objects is removed and the remaining 51 objects are used for training. Table II depicts the probabilities of correct classification (a dihedral is classified as dihedral) and false-alarm (a clutter object is classified as dihedral) for the resolution-dependent and resolution-independent features, as well as for the ICM and LSM segmentation algorithms.

As already suggested by the scatterplots in Figure 13, the proposed resolution-independent features perform a compression in the feature space. This ultimately yields a smaller false-alarm rate. For the simple example considered here, 100% correct classification with 0% false-alarm can be achieved when using resolution-independent features. Further, it is noted that the LSM algorithm performs slightly better than the ICM.

It is noted that in this paper we considered the problem of obtaining features that are independent of signal bandwidth, array aperture and target distance. Target orientation in azimuth and elevation has not been modeled explicitly. Practically this means that the proposed framework assigns separate classes for different orientations of the same object rather than having a single object class that covers all orientations.

It is further noted that we assume perfect knowledge of the wall parameters and consider a homogeneous wall. The proposed general classification scheme is independent of the actual wall removal technique. Its individual steps, however, need to be adjusted when considering highly complicated wall structures. This may include wall removal techniques that are based on electromagnetic modeling of the wall. It also may include a more sophisticated segmentation that includes uncompensated wall effects as an independent class. Finally, the question of robustness of features with respect to wall removal needs to be discussed.

## VI. CONCLUSION

The problem of target classification in the image-domain with application to Through-the-wall radar imaging was addressed. In this application, the imaging system aperture and bandwidth as well as the pixel locations in range and aspect angle can influence the target appearance in the 3D image and as such impact its classification. The paper considered invariance to those parameters through a process of segmentation, feature extraction and discrimination. Statistical as well as geometrical based features have been proposed to discriminate targets from clutter returns in the image domain. Compensation methods aiming at achieving resolution-independent features have been derived and applied to real data measurements. The experimental results demonstrate the usefulness of the proposed methods as desired target returns appear in clusters which are discriminable from clutter returns.



Christian Debes received the M.Sc. and Dr.-Ing. degree in electrical engineering from Technische Universität Darmstadt, Darmstadt, Germany in 2006 and 2010, respectively. He is currently a postdoc in the Institute of Telecommunications, Signal Processing Group at Technische Universität Darmstadt. His research interests include detection, classification and image processing with applications to radar imaging



Jürgen Hahn received his B.Sc. degree in computer engineering from the Department of Electrical Engineering at Technische Universität Darmstadt, Darmstadt, Germany in 2009. Currently, he is working towards his M.Sc degree with an emphasis on statistical signal processing and machine learning.



Abdelhak Zoubir is an IEEE Fellow and an IEEE Distinguished Lecturer (2010-2011). He received his Dr.-Ing. from Ruhr-Universität Bochum, Germany in 1992. He was with Queensland

University of Technology, Australia from 1992 to 1998 where he was an Associate Professor. In 1999, he joined Curtin University of Technology, Australia, as Professor of Telecommunications and was Interim Head of the School of Electrical & Computer Engineering from 2001 until 2003. Since 2003, he has been Professor and Head of the Signal Processing Group at Technische Universität Darmstadt, Germany.

His research interest lies in statistical methods for signal processing applied to telecommunications, sonar, radar, automotive safety and diagnosis, and biomedicine. He published over 300 papers in these areas. Dr Zoubir was Technical Chair of the 11th IEEE Workshop on Statistical Signal Processing (SSP 2001) held in Singapore in 2001, General Co-Chair of the 3rd IEEE International Symposium on Signal Processing & Information Technology (ISSPIT 2003) held in Darmstadt, Germany, General Co-Chair of the 5th IEEE Sensor Array and Multi-Channel Signal Processing Workshop (SAM 2008), held in Darmstadt in July 2008 and Member of the Technical Committee as Co-Chair for Plenary Sessions for ICASSP-08, held in Las Vegas, USA. He is the Technical Co-Chair of ICASSP-14 to be held in Florence, Italy.

Dr Zoubir was an Associate Editor of the IEEE Transactions on Signal Processing from 1999-2005 and has been a Member of the Senior Editorial Board of the IEEE Journal on Selected Topics in Signal Processing since 2009. He is the Chair of the IEEE SPS Technical Committee Signal Processing Theory and Methods (SPTM), (he was its Vice-Chair from 2008-2009 and a member from 2002-2007). He has been a Member of the IEEE SPS Technical Committee Sensor Array and Multi-Channel Signal Processing (SAM) since 2007 and was a Member of the IEEE SPS Technical Committee on Signal Processing Education (SpEd) from 2006-2008. He has been a Member of the Board of Directors of the European Association for Signal Processing (EURASIP) since 2009. Dr Zoubir co-authored the papers that received the IEEE SPS Young Author Best Paper Award in 2003 and 2011.



Dr. Moeness Amin, received his Ph.D. degree in 1984 from University of Colorado, in Electrical Engineering. He has been on the Faculty of the Department of Electrical and Computer Engineering at Villanova University since 1985. In 2002, he became the Director of the Center for Advanced Communications, College of Engineering.

Dr. Amin is the Recipient of the 2009 Individual Technical Achievement Award from the European Association of Signal Processing, and the Recipient of the 2010 NATO Scientific Achievement Award. He is a Fellow of the Institute of Electrical and Electronics Engineers (IEEE), Fellow of the International Society of Optical Engineering; and a Fellow of the Institute of Engineering and Technology (IET). Dr. Amin is a Recipient of the IEEE Third Millennium Medal; Recipient of the Chief of Naval Research Challenge Award, 2010; Distinguished Lecturer of the IEEE Signal Processing Society, 2003-2004; Active Member of the Franklin Institute Committee on Science and the Arts; Recipient Villanova University Outstanding Faculty Research Award, 1997; and the Recipient of the IEEE Philadelphia Section Award, 1997. He is a member of IEEE, SPIE, EURASIP, ION, Eta Kappa Nu, Sigma Xi, and Phi Kappa Phi.

Dr. Amin has over 450 journal and conference publications in the areas of Wireless Communications, Time-Frequency Analysis, Smart Antennas, Waveform Design and Diversity, Interference Cancellation in Broadband Communication Platforms, Anti-Jam GPS, Target Localization and Tracking, Direction Finding, Channel Diversity and Equalization, Ultrasound Imaging and Radar Signal Processing. He is a recipient of seven best paper awards.

Dr. Amin currently serves on the Overview Board of the IEEE Transactions on Signal Processing. He also serves on the Editorial Board of the EURASIP Signal Processing Journal. He was a Plenary Speaker at ICASSP 2010. Dr. Amin was the Special Session Co-Chair of the 2008 IEEE International Conference on Acoustics, Speech, and Signal Processing.

He was the Technical Program Chair of the 2nd IEEE International Symposium on Signal<sup>24</sup> Processing and Information Technology, 2002. Dr. Amin was the General and Organization Chair of the IEEE Workshop on Statistical Signal and Array Processing, 2000. He was the General and Organization Chair of the IEEE International Symposium on Time-Frequency and Time-Scale Analysis, 1994. He was an Associate Editor of the IEEE Transactions on Signal Processing during 1996-1998. He was a member of the IEEE Signal Processing Society Technical Committee on Signal Processing for Communications during 1998-2002. He was a Member of the IEEE Signal Processing Society Technical Committee on Statistical Signal and Array Processing during 1995-1997.

Dr. Amin was the Guest Editor of the Journal of Franklin Institute September-08 Special Issue on Advances in Indoor Radar Imaging. He was a Guest Editor of the IEEE Transactions on Geoscience and Remote Sensing May-09 Special Issue on Remote Sensing of Building Interior, and a Guest Editor of the ET Signal Processing December-09 Special Issue on Time-Frequency Approach to Radar Detection, Imaging, and Classification.



## REFERENCES

- [1] M. G. Amin, Ed., *Through-the-Wall Radar Imaging*, CRC Press, 2010.
- [2] M. Amin and K. Sarabandi (Guest Editors), “Special issue on remote sensing of building interior,” *IEEE Transactions on Geoscience and Remote Sensing*, vol. 47, no. 5, 2009.
- [3] M. Amin (Guest Editor), “Special issue: Advances in indoor radar imaging,” *Journal of the Franklin Institute*, vol. 345, no. 6, 2008.
- [4] E. Baranoski and F. Ahmad (Session Chairs), “Special session on through-the-wall radar imaging,” in *IEEE International Conference on Acoustics, Speech and Signal Processing*, 2008.
- [5] E. Baranoski, “Through-wall imaging: Historical perspective and future directions,” *Journal of the Franklin Institute*, vol. 345, no. 6, pp. 556–569, 2008.
- [6] F. Ahmad and M.G. Amin, “Noncoherent approach to through-the-wall radar localization,” *IEEE Transactions on Aerospace and Electronic Systems*, vol. 42, no. 4, pp. 1405–1419, 2006.
- [7] F. Ahmad and M.G. Amin, “Multi-location wideband synthetic aperture imaging for urban sensing applications,” *Journal of the Franklin Institute*, vol. 345, no. 6, pp. 618–639, 2008.
- [8] M. Dehmollaian and K. Sarabandi, “Refocusing through building walls using synthetic aperture radar,” *IEEE Transactions on Geoscience and Remote Sensing*, vol. 46, no. 6, pp. 1589–1599, 2008.
- [9] Y.-S. Yoon and M.G. Amin, “High-resolution through-the-wall radar imaging using beamspace MUSIC,” *IEEE Transactions on Antennas and Propagation*, vol. 56, no. 6, pp. 1763–1774, 2008.
- [10] R. N. Narayanan, “Through-wall radar imaging using UWB noise waveforms,” *Journal of the Franklin Institute*, vol. 345, no. 6, pp. 659–678, 2008.
- [11] C. Debes, M.G. Amin, and A.M. Zoubir, “Target detection in single- and multiple-view through-the-wall radar imaging,” *IEEE Transactions on Geoscience and Remote Sensing*, vol. 47(5), pp. 1349 – 1361, 2009.
- [12] C. Debes, J. Riedler, M.G. Amin, and A.M. Zoubir, “Iterative target detection approach for through-the-wall radar imaging,” in *Proc. of the IEEE International Conference on Acoustics, Speech and Signal Processing*, 2009, pp. 3061 – 3064.
- [13] C. Debes, M.G. Amin, and A.M. Zoubir, “Target detection in multiple-viewing through-the-wall radar imaging,” in *Proceedings of the IEEE International Geoscience and Remote Sensing Symposium*, 2008, pp. 173–176.
- [14] C. Debes, A.M. Zoubir, and M.G. Amin, “Optimal decision fusion in through-the-wall radar imaging,” in *Proceedings of the IEEE International Workshop on Statistical Signal Processing*, 2009, pp. 761–764.
- [15] B. G. Mobasseri and Z. Rosenbaum, “3D classification of through-the-wall radar images using statistical object models,” in *Proceedings of the IEEE Workshop on Image Analysis and Interpretation*, 2008, pp. 149–152.
- [16] C. Debes, J. Hahn, M.G. Amin, and A.M. Zoubir, “Feature extraction in through-the-wall radar imaging,” in *Proceedings of the IEEE International Conference on Acoustics, Speech and Signal Processing*, 2010, pp. 3562 – 3565.
- [17] M. P. Hayes and P. T. Gough, “Synthetic aperture sonar: A review of current status,” *IEEE Journal of Oceanic Engineering*, vol. 34, no. 3, pp. 207–224, 2009.
- [18] R. Fandos and A. Zoubir, “Optimal feature set for automatic detection and classification of underwater objects in SAS images,” *IEEE Journal of Selected Topics in Signal Processing*, , no. 99, 2010, Early Access.
- [19] Y. Hua, F.A. Baqai, Y. Zhu, and D.J. Heilbronn, “Imaging of point scatterers from step-frequency ISAR data,” *IEEE Transactions on Aerospace and Electronic Systems*, vol. 29, no. 1, pp. 195–205, 1993.

- [20] R.M. Nuthalapati, “High resolution reconstruction of ISAR images,” *IEEE Transactions on Aerospace and Electronic Systems*, vol. 28, no. 2, pp. 462–472, 1992.
- [21] G. Alli and D. DiFilippo, *Through-the-Wall Radar Imaging*, chapter Beamforming for Through-the-Wall Radar Imaging, CRC Press, 2010.
- [22] M.A. Richards, *Fundamentals of Radar Signal Processing*, McGraw-Hill, 2005.
- [23] D. Massonnet and J.-C. Souyris, *Imaging with Synthetic Aperture Radar*, CRC Press, 2008.
- [24] J. Besag, “On the statistical analysis of dirty pictures,” *Journal of the Royal Statistical Society B*, vol. 48, pp. 259–302, 1986.
- [25] S. Osher and J.A. Sethian, “Fronts propagating with curvature dependent speed: Algorithms based on hamilton-jacobi formulations,” *Journal of Computational Physics*, vol. 79, no. 1, pp. 12–49, 1988.
- [26] J.-S. Lee and I. Jurkevich, “Segmentation of SAR images,” *IEEE Transactions on Geoscience and Remote Sensing*, vol. 27, no. 6, pp. 674 – 680, 1989.
- [27] N.D.A. Mascarenhas and A.C. Frery, “SAR image filtering with the ICM algorithm,” in *Proceedings of the IEEE International Geoscience and Remote Sensing Symposium*, 1994, vol. 4, pp. 2185–2187.
- [28] Z. Belhadj, A. Saad, S. El Assad, J. Saillard, and D. Barba, “Comparative study of some algorithms for terrain classification using SAR images,” in *Proceedings of the IEEE International Conference on Acoustics, Speech, and Signal Processing*, 1994, pp. 165–168.
- [29] F. Galland, J.-M. Nicolas, H. Sportouche, M. Roche, F. Tupin, and P. Refregier, “Unsupervised synthetic aperture radar image segmentation using fisher distributions,” *IEEE Transactions on Geoscience and Remote Sensing*, vol. 47, no. 8, pp. 2966–2972, 2009.
- [30] G.-S. Xia, C. He, and H. Sun, “Integration of synthetic aperture radar image segmentation method using markov random field on region adjacency graph,” *IET Radar, Sonar and Navigation*, vol. 1, no. 5, pp. 348–353, 2007.
- [31] G. Winkler, *Image Analysis, Random Fields and Markov Chain Monte Carlo Methods: A Mathematical Introduction*, Springer, 2004.
- [32] G. Al-Osaimi and A. El-Zaart, “Minimum cross entropy thresholding for SAR images,” in *Proceedings of the International Conference on Information and Communication Technologies*, 2008.
- [33] R.C. Gonzales and R.E. Woods, *Digital Image Processing*, Prentice Hall, 2001.
- [34] J.-S. Lee, K.W. Hoppel, S.A. Mango, and A.R. Miller, “Intensity and phase statistics of multilook polarimetric and interferometric SAR imagery,” *IEEE Transactions on Geoscience and Remote Sensing*, vol. 32, no. 5, pp. 1017–1028, 1994.
- [35] C. Debes, J. Riedler, A. M. Zoubir, and M. G. Amin, “Adaptive target detection with application to through-the-wall radar imaging,” *IEEE Transactions on Signal Processing*, vol. 58, no. 11, pp. 5572–5583, 2010.
- [36] M. Kass, A. Witkin, and D. Terzopoulos, “Snakes: Active contour models,” *International Journal of Computer Vision*, vol. 1, no. 4, pp. 321–331, 1988.
- [37] Stanley J. Osher and Ronald P. Fedkiw, *Level Set Methods and Dynamic Implicit Surfaces*, Springer, 1 edition, October 2002.
- [38] V. Caselles, R. Kimmel, and G. Sapiro, “Geodesic active contours,” *International Journal of Computer Vision*, vol. 22, no. 1, pp. 61–79, 1997.
- [39] Y. Zhang, B.J. Matuszewski, L.-K. Shark, and C.J. Moore, “Medical image segmentation using new hybrid level-set method,” in *Proceedings of the International Conference on BioMedical Visualization*, 2008, pp. 71–76.

- [40] A.H. Barr, “Superquadrics and angle-preserving transformations,” *IEEE Computer Graphics and Applications*, vol. 1, no. 1, pp. 11–23, 1981.
- [41] F. Solina and R. Bajcsy, “Recovery of parametric models from range images: the case for superquadrics with global deformations,” *IEEE Transactions on Pattern Analysis and Machine Intelligence*, vol. 12, no. 2, pp. 131–147, 1990.
- [42] W. H. Press, B. P. Flannery, S. A. Teukolsky, and W. T. Vetterling, *Numerical Recipes*, Cambridge University Press, 1989.
- [43] L. E. Scales, *Introduction to non-linear optimization*, Springer-Verlag New York, Inc., 1985.
- [44] J. Craig, *Introduction to Robotics: Mechanics and Control*, Addison-Wesley Longman Publishing Co., Inc., Boston, MA, USA, 1989.
- [45] T.W. Sederberg and S.R. Parry, “Free-form deformation of solid geometric model,” *SIGGRAPH*, pp. 151 – 160, 1986.
- [46] L. Chevalier, F. Jaillet, and A. Baskurt, “Segmentation and superquadric modeling of 3d objects,” in *International Conference on Computer Graphics, Visualization and Computer Vision*, 2003.
- [47] B. Silverman, *Density Estimation for Statistics and Data Analysis*, Chapman & Hall, 1986.
- [48] T.W. Anderson, *An Introduction to Multivariate Statistical Analysis*, Wiley-Interscience, 2003.

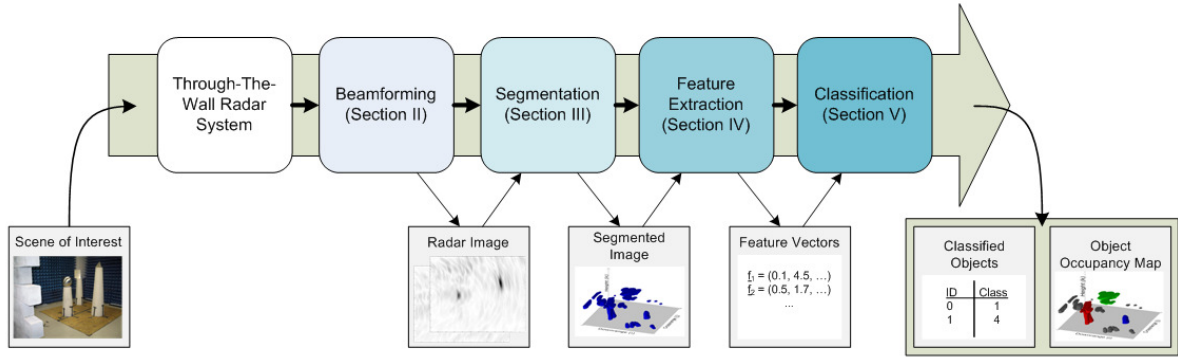


Fig. 1. Through-the-Wall Radar Imaging Classification chain

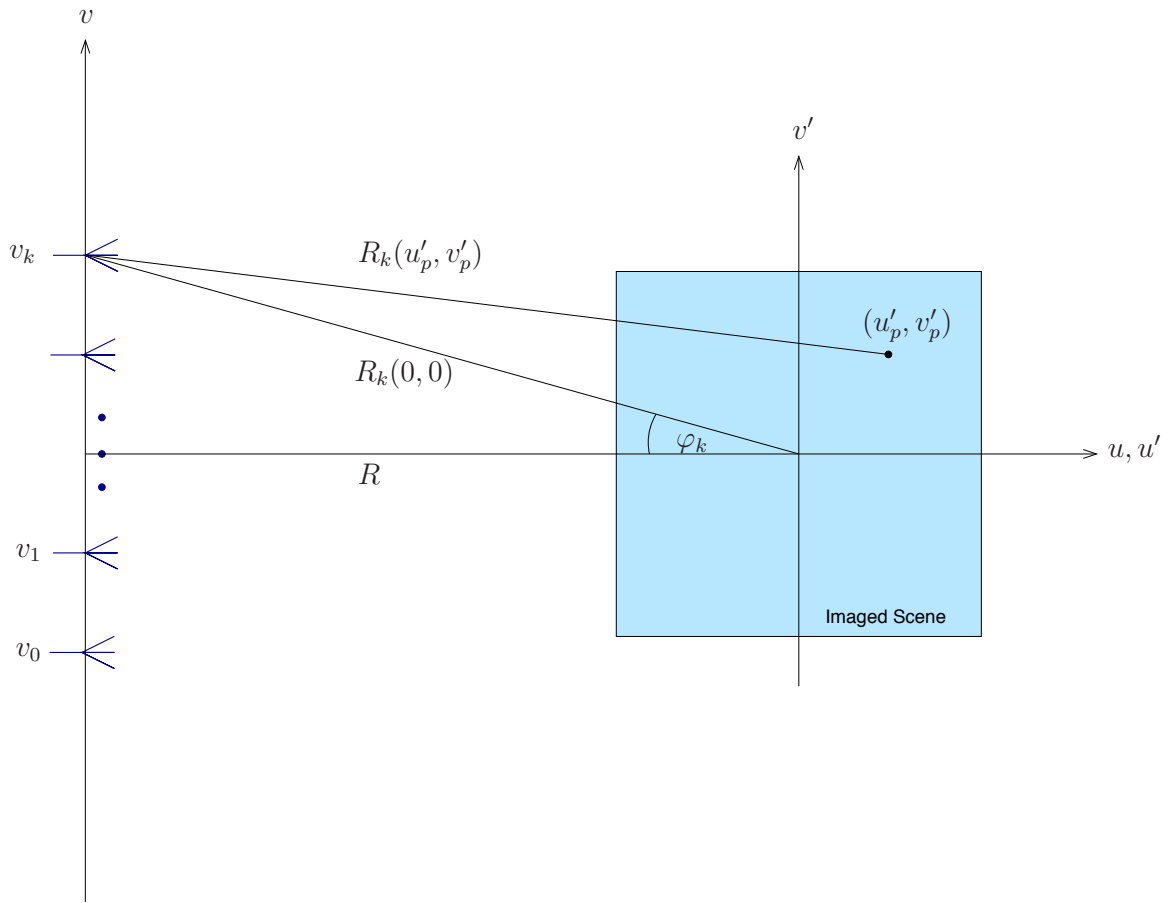


Fig. 2. Beamforming scheme for high resolution radar imaging

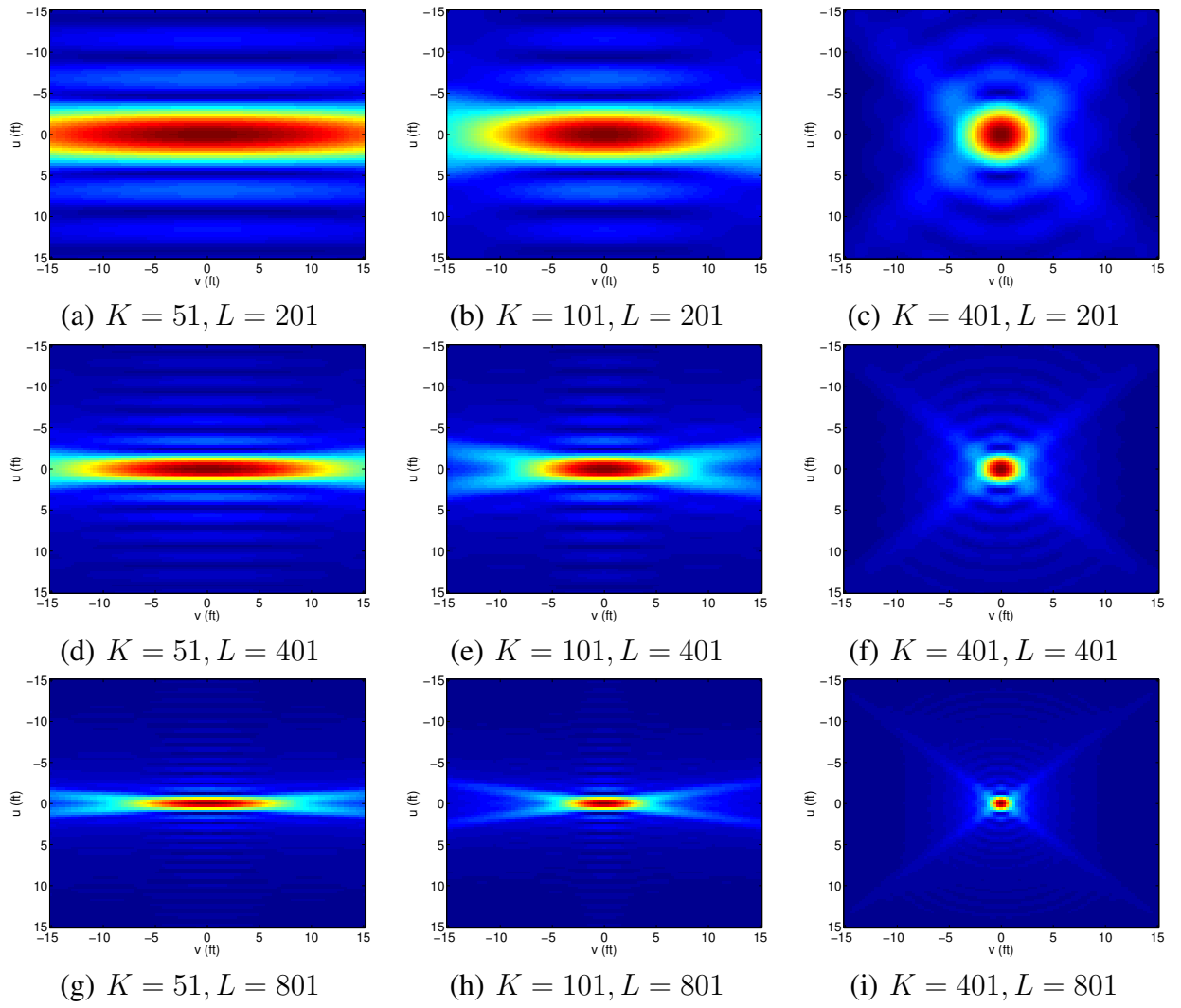


Fig. 3. System point spread function varying with resolution

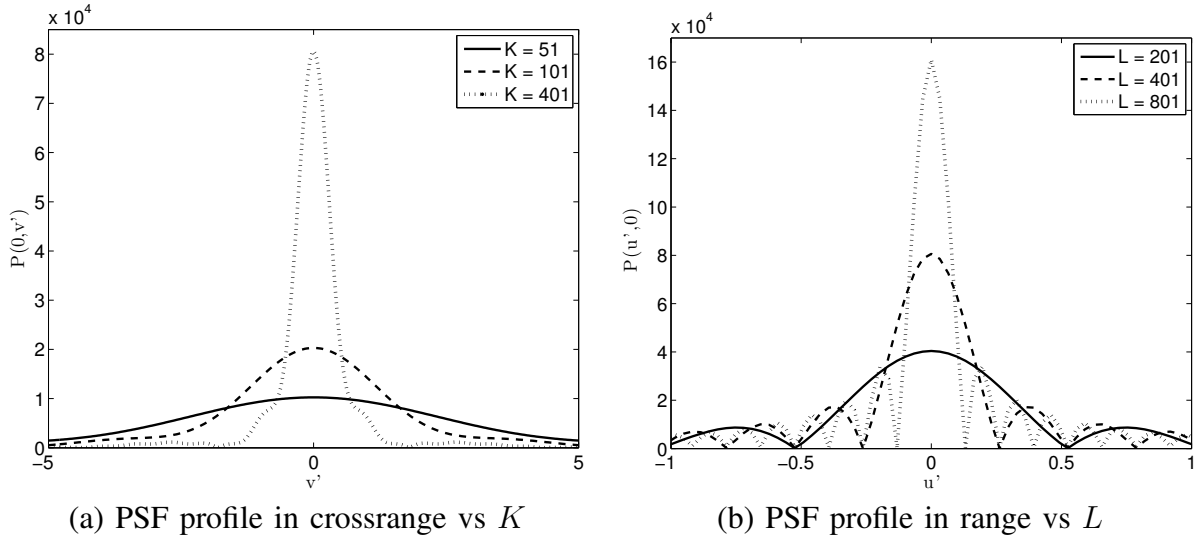


Fig. 4. PSF cuts at 0 range and crossrange

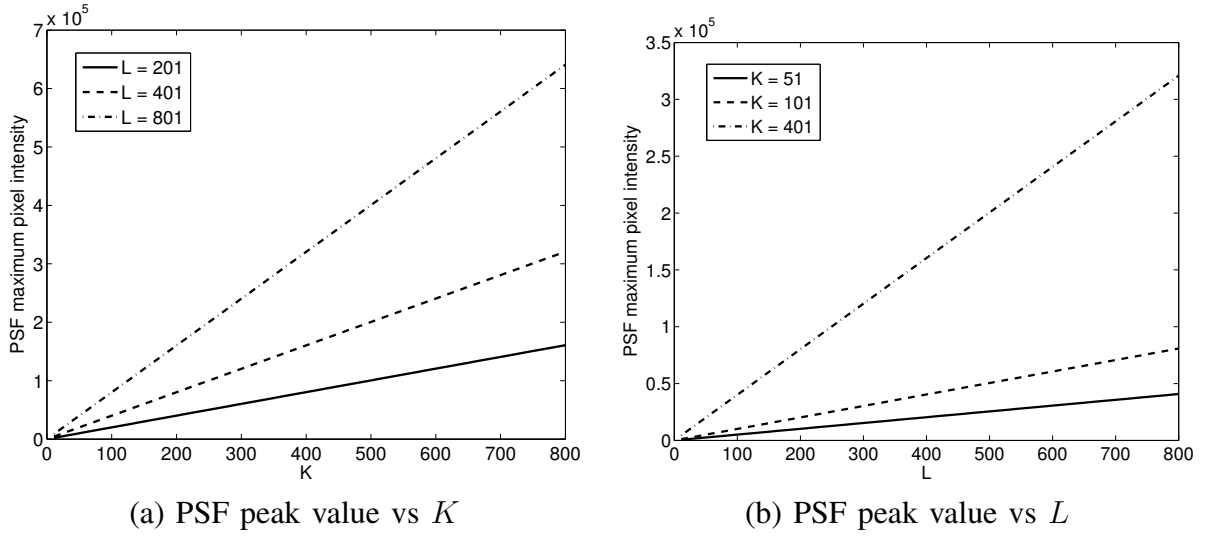


Fig. 5. Linear relationship between the maximum pixel intensity and the number of array elements and bandwidth

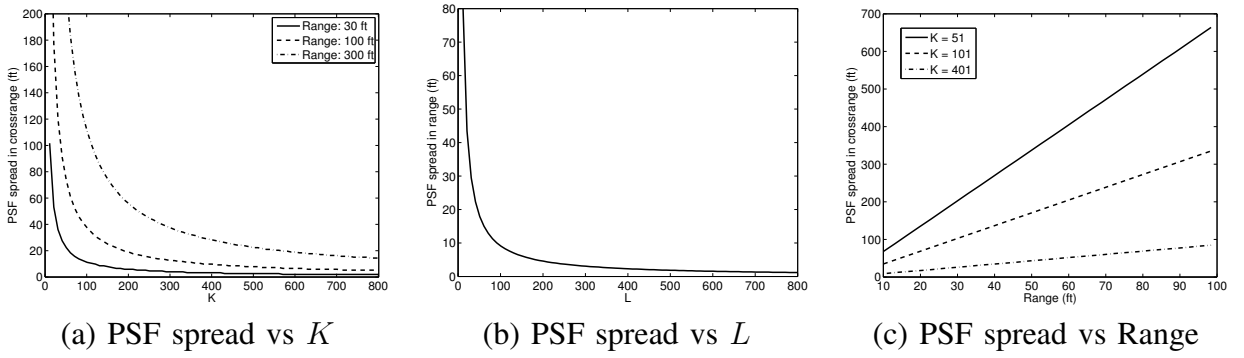


Fig. 6. The PSF spread as a function of the number of array elements, bandwidth and range

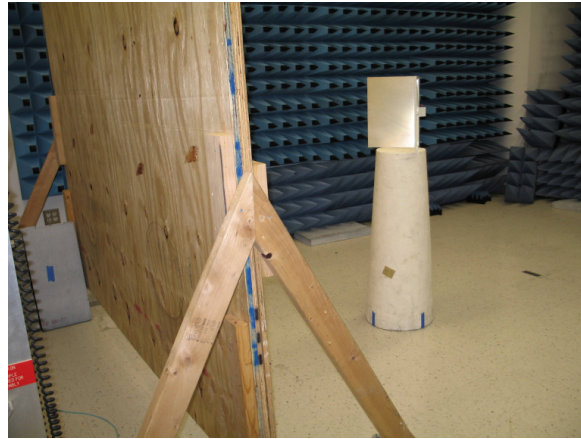


Fig. 7. Experimental setup

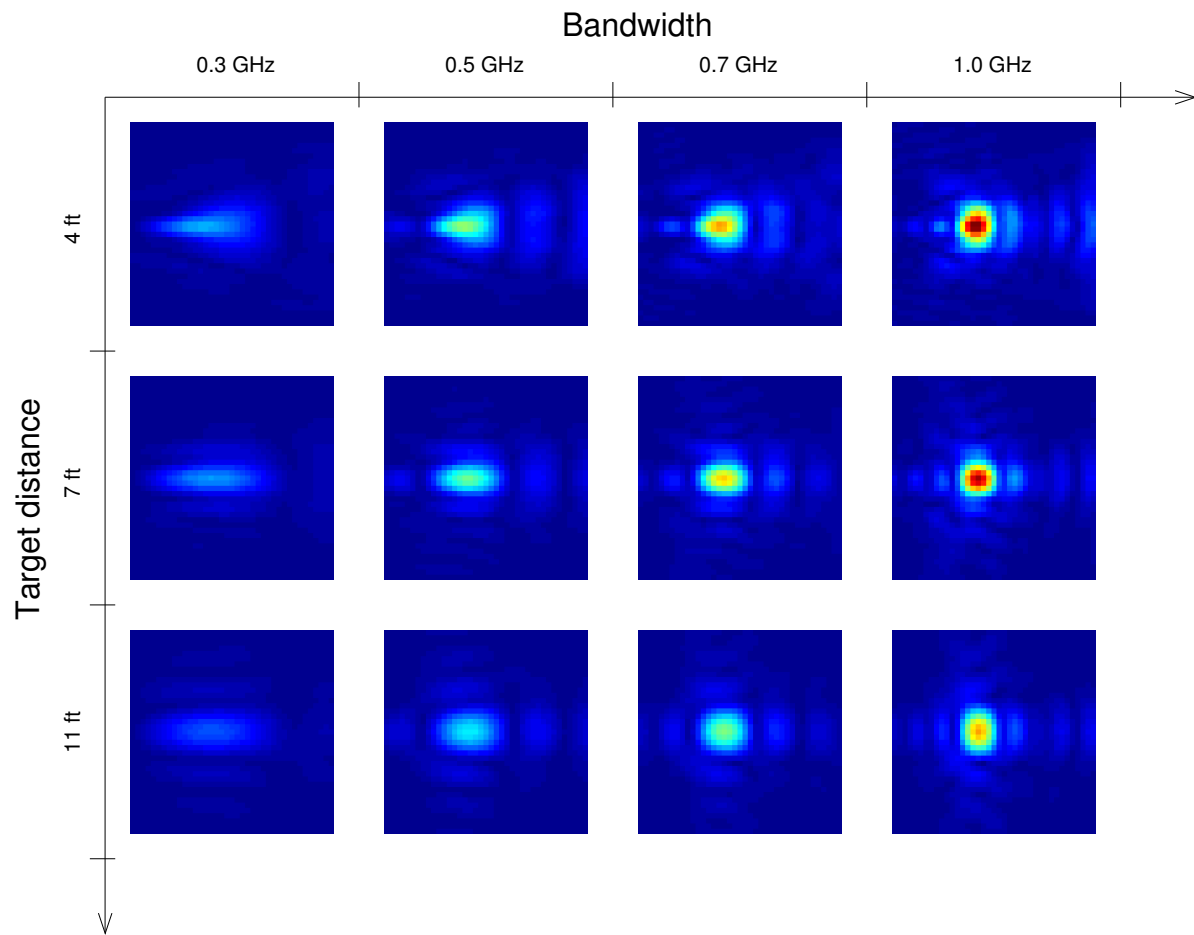


Fig. 8. Target image changes with resolution

		Resolution-Dependent	Resolution-Independent
ICM	Correct Classification	100%	100%
	False Alarm	10%	2.5%
LSM	Correct Classification	100%	100%
	False Alarm	7.5%	0%

TABLE II  
CLASSIFICATION RESULTS

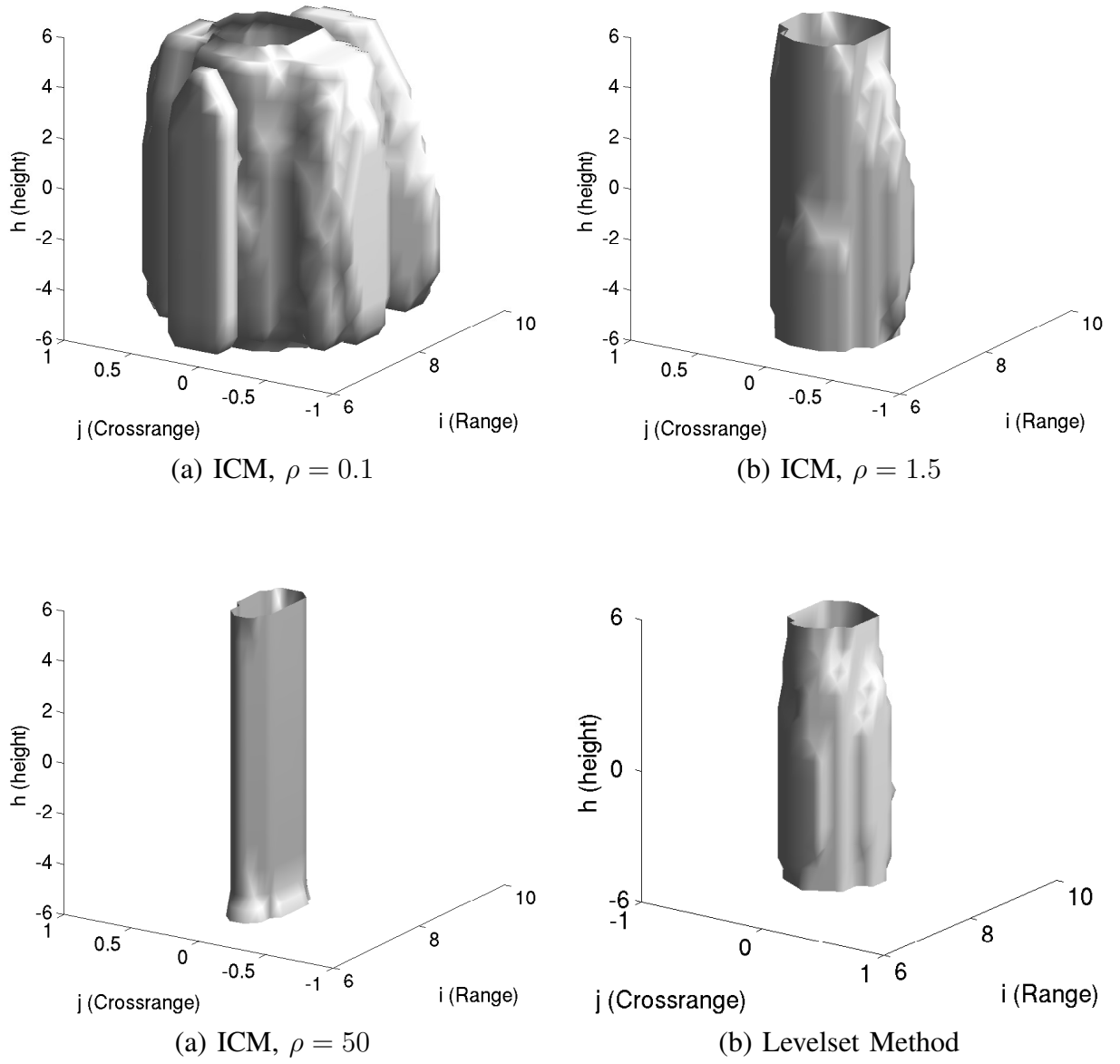


Fig. 9. Segmentation Results

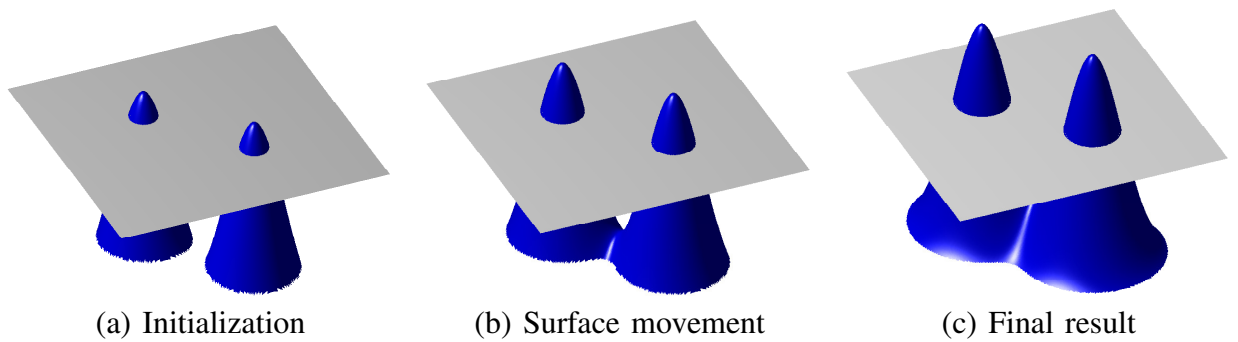
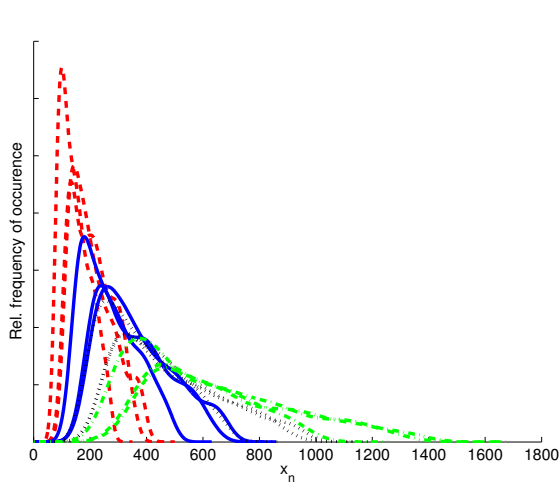
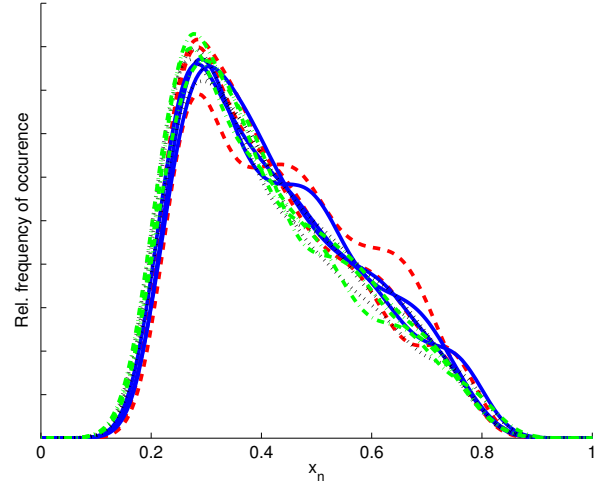


Fig. 10. Principle of the Level Set Method

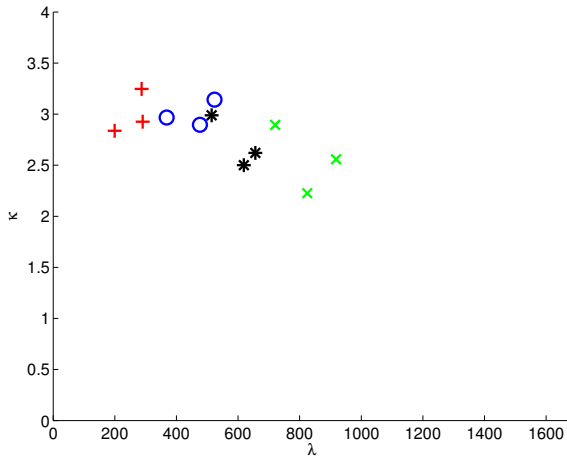




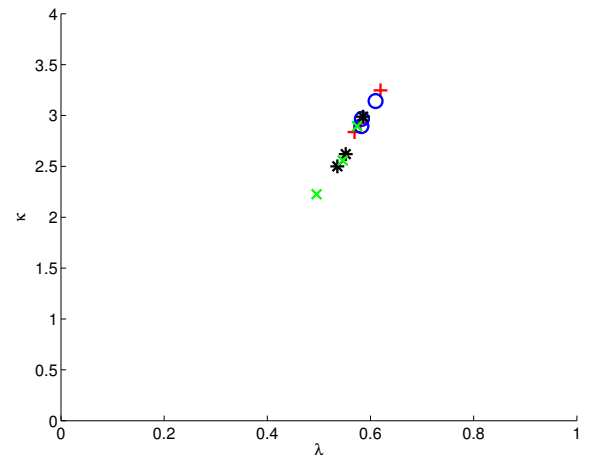
(a) Target histograms, uncompensated



(b) Target histograms, compensated

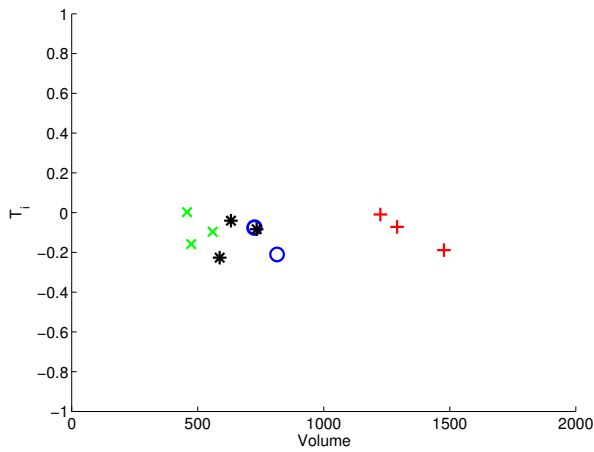


(c) Parameter estimates, uncompensated

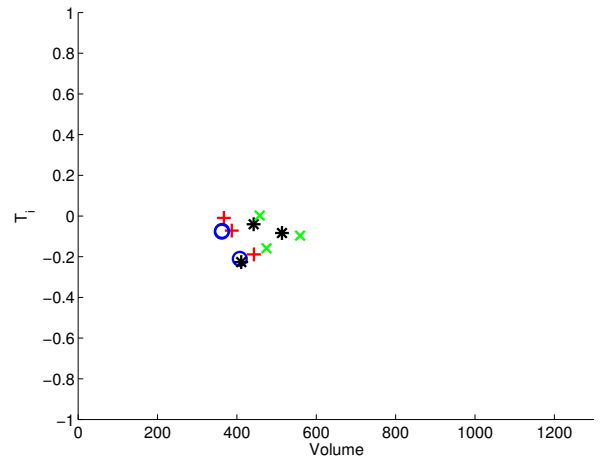


(d) Parameter estimates, compensated

Fig. 11. Statistical feature compensation



(a) Superquadric parameters, uncompensated



(b) Superquadric parameters, compensated

Fig. 12. Geometric feature compensation

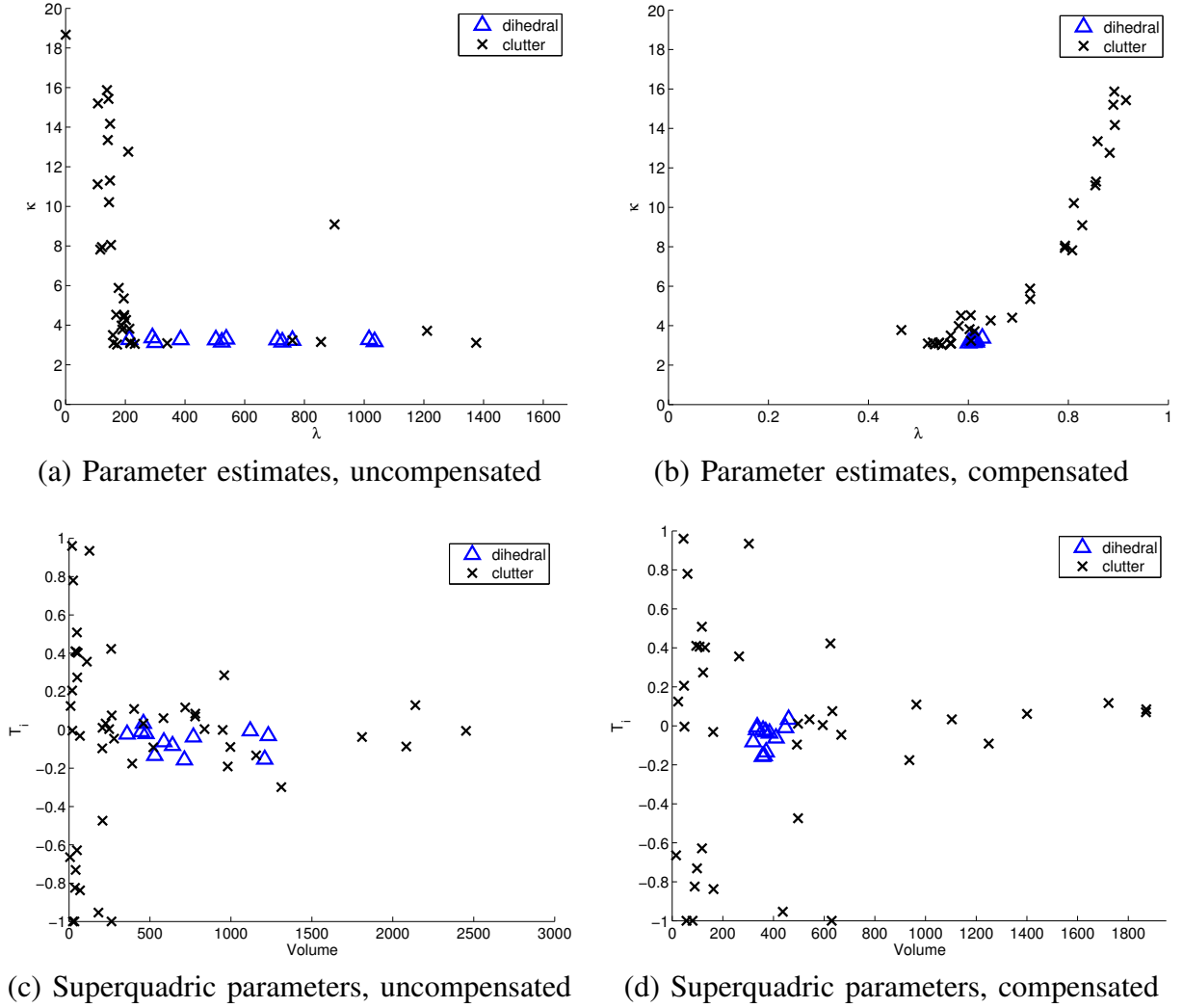


Fig. 13. Target/clutter clusters